

Growth Kinetics and Magnetic Property of Single-Crystal Fe Nanowires Grown via Vapor–Solid Mechanism Using Chemically Synthesized FeO Nanoparticle Catalysts

Takashi Yanase,^{*,†} Uika Ogihara,[‡] Yoshihiro Awashima,[†] Takeshi Yanagida,[§] Kazuki Nagashima,[§] Taro Nagahama,[†] and Toshihiro Shimada[†]

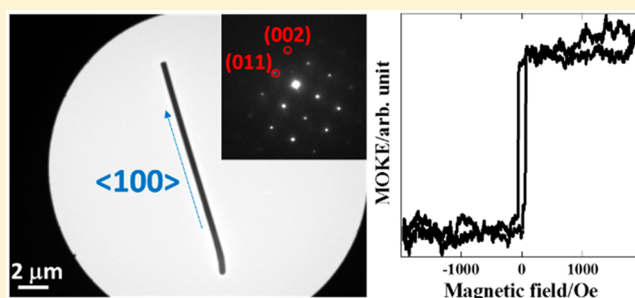
[†]Division of Applied Chemistry, Faculty of Engineering, Hokkaido University, Kita 13 Nishi 8 Kita-ku, Sapporo 060-8628, Japan

[‡]Graduate School of Chemical Sciences and Engineering, Hokkaido University, Kita 13 Nishi 8 Kita-ku, Sapporo 060-8682, Japan

[§]Laboratory of Integrated Nanostructure Materials, Institute of Materials Chemistry and Engineering, Kyushu University, 6-1 Kasuga-koen, Kasuga, Fukuoka 816-8580, Japan

Supporting Information

ABSTRACT: Single-crystal Fe nanowires (NWs) were synthesized on SiO₂/Si substrates by chemical vapor deposition (CVD) using a two-flow system in the presence of FeO nanoparticles as catalysts. Transmission electron microscopy observations and an electron diffraction analysis revealed that the NW was defect-free α -Fe (bcc structure) oriented in the $\langle 100 \rangle$ direction. A plausible mechanism of the Fe NW growth is suggested based on the observations of the morphology and characteristic diameter of the Fe NW. We found that the NWs became polycrystalline when their diameter was approximately 100 nm. The excellent crystal quality of the single-crystal NW was confirmed by electron diffraction and the residual resistance ratio. Magnetic uniformity and a strong shape-anisotropic behavior of magnetization were observed by measuring the hysteresis loop and the angle dependence of the magneto-optical Kerr effect, respectively.



INTRODUCTION

Iron is recognized as one of the most critical elements from ancient times to now due to its abundance, toughness, well-established processing, and magnetism. Therefore, it is widely used in human society, for example, construction materials, automobiles, and magnets. Recent nanotechnology has opened the opportunities for the well-known materials to be improved and tune their properties, for example, a large variety of single-crystal nanowires (NWs) has been studied due to their superior properties derived from the 1D geometry. In particular, semiconducting NWs, such as Si,^{1–3} GaN,⁴ GaAs,⁵ ZnO,^{6,7} and InAs,⁸ have been intensively investigated for practical applications as field-effect transistors,^{9,10} supercapacitors,³ and sensors^{11,12} because the semiconducting NWs can be rationally configured or structured by chemical vapor deposition (CVD) with foreign nanoparticles via a vapor–liquid–solid (VLS) mechanism. Ferromagnetic NWs (FMNWs) have also attracted considerable attention due to not only the interest in magnetic anisotropy^{13–19} but also potential applications in spin devices.²⁰ Since the growth of FMNWs by CVD is still limited due to a vapor–solid (VS) mechanism that remains unclear regarding the microscopic processes of the NW formation, most FM NWs were preferably fabricated by electrodeposition using an anodic alumina oxide template¹⁸ or etching of a film using

nanolithography.^{14,15} However, the polycrystalline nature, rough surfaces of the NW walls, internal stress, and inevitable contamination degrade the magnetic properties of the NWs. The costly process is another disadvantage of the template and nanolithography methods. Therefore, it is crucial to establish a method for the growth of single-crystal FMNWs using a feasible and scalable CVD approach.

Our research group has revisited the Fe whisker growth that was studied in the 1960s–1970s,^{21–23} then synthesized the single-crystal Fe NWs on an Al₂O₃ substrate with Au nanoparticles as the catalyst²⁴ and on a YSZ substrate without a catalyst.²⁵ If one can avoid using expensive single-crystal substrates, such as Al₂O₃ and YSZ, the CVD becomes more realistic as a practical method to synthesize single-crystal Fe NWs. In this study, we synthesized single-crystal Fe NWs on SiO₂/Si substrates using FeO nanoparticles as a catalyst by thermal CVD based on the simple reduction of FeCl₂ with H₂.

EXPERIMENTAL SECTION

Figure 1 shows a schematic illustration of the home-built CVD equipment with a two-flow system for the growth of the Fe NWs in

Received: August 29, 2019

Revised: October 15, 2019

Published: October 21, 2019

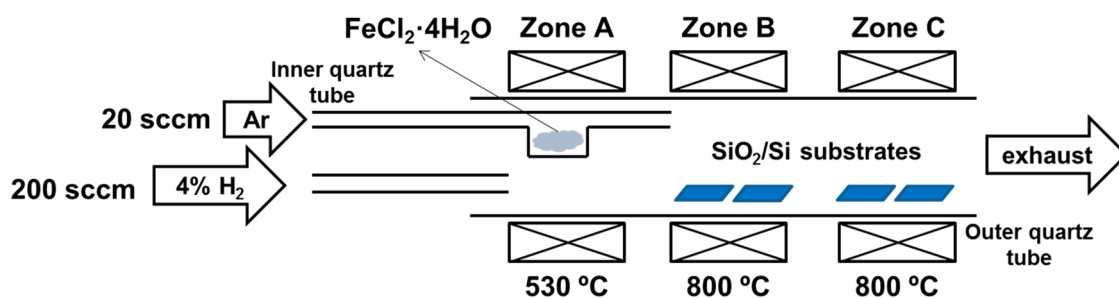


Figure 1. Schematic illustration of the two-flow CVD equipment used for the growth of the Fe NWs.

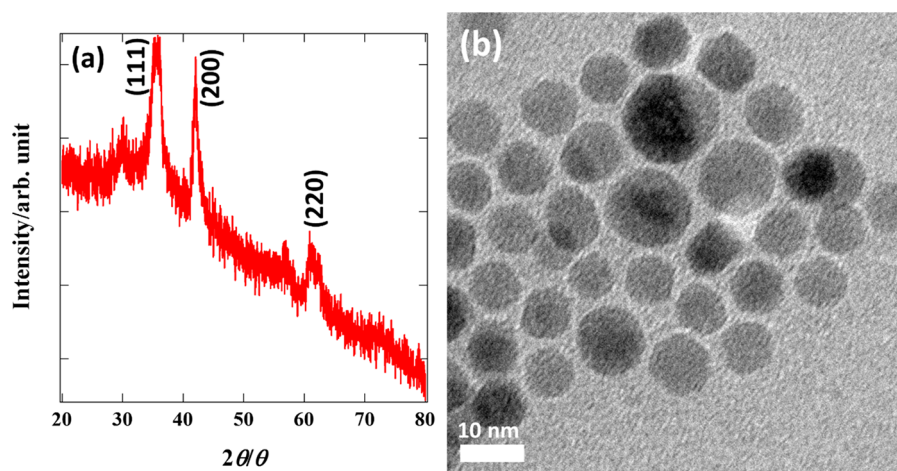


Figure 2. (a) XRD pattern and (b) TEM image of FeO nanoparticles. FeO nanoparticles were dispersed in hexane and dip-coated on the substrates under sonication.

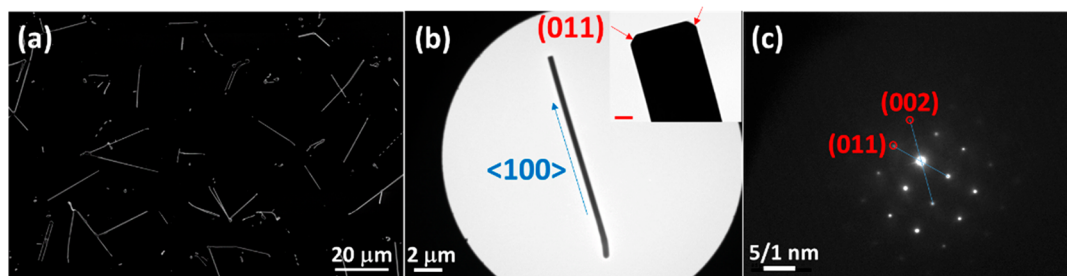


Figure 3. (a) SEM image of Fe NWs grown on SiO₂/Si using FeO nanoparticles as catalysts. (b) TEM image of a single Fe NW. The inset shows the detailed morphology of the tip part. The scale bar in the inset of (b) is 100 nm. (c) Electron diffraction pattern obtained from the Fe NW indicates the Fe NWs defect-free single crystal.

this study. The CVD equipment was partly modified to improve its controllability and reproducibility compared to previous reports.^{24,25} Our CVD system includes a furnace with three temperature-controllable zones, an outer quartz tube with a diameter of 28 mm, and an inner quartz tube with a diameter of 6 mm. Each zone of the furnace was labeled zone A, zone B, and zone C from upstream. FeCl₂·4H₂O powder (0.2 g, Purity 99%, Kanto Chemical Co., Inc.) was placed in a pocket of the inner quartz tube as shown by the arrow in Figure 1. The paths through the inner quartz tube and the outer quartz tube were called the FeCl₂ line and H₂ line, respectively. The introduction of the inner quartz tube hinders the reduction of the FeCl₂ powder by the H₂ gas during the CVD, while most of the reported studies of the CVD-grown metal NWs ignored the direct reduction of the source materials due to the single-flow system.^{16,21,22} In our CVD system, FeCl₂ vapor can be continuously and stably supplied to the substrates for the growth of the Fe NWs. Furthermore, the ratio of the partial vapor pressures of FeCl₂ and H₂ can be optimized to guarantee the reproducibility by the mass flow

controllers that are separately equipped with both the FeCl₂ line and the H₂ line.

SiO₂(200 nm)/Si wafers cut into 1 × 1 cm² pieces were used as the substrates. The SiO₂/Si substrates were cleaned by the Radio Corporation of America (RCA) cleaning method to remove any metal and organic surface contaminants.²⁶ After the RCA cleaning, FeO nanoparticles dispersed in a hexane solution were dip-coated under sonication. The FeO nanoparticles were synthesized using a heat-up method according to ref 27. The nanoparticles were identified as FeO by X-ray diffraction (XRD) as shown in Figure 2(a). A TEM image shown in Figure 2(b) shows the narrow size distribution of the nanoparticles (8–15 nm). The FeO nanoparticles must be handled under an inert atmosphere to avoid oxidation because FeO is sensitive to air.²⁷

The CVD procedure to synthesize the Fe NWs was as follows. Immediately after the SiO₂/Si substrates with FeO nanoparticles were placed in the outer quartz tube, the inside of the whole CVD system was evacuated. When the inside pressure reached lower than 10 Pa, the quartz tube was filled with Ar gas through the FeCl₂ line. FeCl₂

$4\text{H}_2\text{O}$ was preannealed at $200\text{ }^\circ\text{C}$ for 45 min to remove the crystal water that may cause oxidation of the Fe NWs. The Ar flow was then stopped, and 4% H_2 (diluted by Ar gas) started to flow at the rate of 20 sccm through the H_2 line. The sequence of the gas introduction is important to avoid direct reduction of the FeCl_2 powder placed in the pocket of the inner quartz tube. When the temperatures of zone A, zone B, and zone C reached 530 , 800 , and $800\text{ }^\circ\text{C}$, respectively, the flow rate in the H_2 line was increased to 200 sccm and the Ar gas began to flow again through the FeCl_2 line at the rate of 20 sccm to supply the FeCl_2 vapor to the substrates. The duration of the gas flow through the FeCl_2 line was defined as the reaction time. After the CVD was carried out for 60 min, Ar flow in the FeCl_2 line was suddenly cut off to stop any undesirable reaction while lowering the temperature. The furnace was naturally cooled to ambient temperature while maintaining the flow of the 4% H_2 gas in order for air not to enter the quartz tube.

The morphology of the Fe NWs was characterized by scanning electron microscopy (SEM; JEOL JSM-6500F and JSM-6390LV) and transmission electron microscopy (TEM; JEOL JEM-2010). The crystallinity and growth axis of the Fe NWs were determined by electron diffraction. Energy dispersive X-ray spectrometers (EDS) equipped with SEM and TEM were used for the elemental analysis. The temperature dependences of the resistivity and magnetoresistance at 9 K were measured using a 4-terminal sensing method. The magnetization of a single Fe NW was measured by a micro-Kerr magnetometer (NEOARK BH-L920WF6-FN).

RESULTS AND DISCUSSION

Figure 3(a) shows an SEM image of Fe NWs grown at random angles on the SiO_2/Si substrate. The diameter and length of the Fe NWs ranged from 100 to 500 nm and from 5 to $35\text{ }\mu\text{m}$, respectively. It was confirmed that nothing had grown on the SiO_2/Si substrate without the FeO nanoparticles, which indicates that the FeO nanoparticles are essential to forming the Fe NWs. An EDS analysis shown in Figure S1 revealed that the NWs were composed of Fe, while Si and O were detected due to the substrate. A single NW was transferred to a TEM grid using a micromanipulator and observed by the TEM to characterize the detailed morphology as shown in Figure 3(b). The growth mechanism of the NWs is generally classified into two types; i.e., (i) VLS mechanism and (ii) VS mechanism. It is straightforward to distinguish the difference between these two mechanisms by observing the tip of an NW. While a round-shaped droplet as a catalyst is always found on the tip by the VLS mechanism,¹ the flat surface of the tip is standard geometry for the NWs grown by the VS mechanism as previously reported for the Sn,²⁸ ZnO,^{6,29} and $\text{W}_{18}\text{O}_{49}$ ³⁰ NWs. The very flat surface as seen in the inset of Figure 3(b) shows that the Fe NWs grew by the VS mechanism. The EDS analysis shows that the NW was composed of Fe and there was no impurity, such as Cl and O, which illustrates that the FeO (catalyst) and FeCl_2 were completely reduced to Fe by the H_2 (see Figure S2). The Cu peaks were always found and originated from the TEM grid. An electron diffraction analysis shown in Figure 3(c) revealed that the NW was the defect-free single-crystal $\alpha\text{-Fe}$ (bcc structure) and the growth direction was $\langle 100 \rangle$. The growth axis of the NW is consistent with a previous report in the 1970s^{21,22} that studied Fe whiskers. While Fe whiskers were preferably grown along the $\langle 110 \rangle$ and $\langle 112 \rangle$ directions when the pure iron boat was used as a substrate, iron oxide particles promoted the growth of the $\langle 100 \rangle$ oriented Fe whiskers. Since we used FeO nanoparticles as the catalyst for the growth of the Fe NWs, the Fe NWs grew along the $\langle 100 \rangle$ axis. The orientation of the sidewalls was determined as $\{100\}$ from the TEM image and the diffraction

pattern. The d value (0.144 nm) calculated from a diffraction spot of (002) is approximately equal to that of the bulk $\alpha\text{-Fe}$ (0.1433 nm). No diffraction spot derived from FeO illustrates that the FeO nanoparticle was totally reduced to Fe. The truncated tip rim seems to be general and probably plays a crucial role in the NW growth because the same geometric structure was also observed for the different NWs as shown in Figure S3. Based on the combined results of the TEM image and the diffraction pattern, the crystallographic orientation of the truncated tip rim is assignable to the (011) planes as indicated in the inset of Figure 3(b) by the red arrows. The details of the growth mechanism are discussed in the next section.

The VS mechanism can be divided into two growth modes; i.e., (i) tip growth and (ii) base growth. These two growth modes can be distinguished by observing the variation in the diameter of an NW, called the characteristic diameter (or radius), when the growth temperature is changed during the CVD. It is well-known that the characteristic diameter is a monotonically increasing function of only the reaction temperature as long as the flux of the reactants is maintained when the NWs grow by the VS mechanism.^{29,31} In order to reveal whether tip growth or base growth is true, we carried out a two-step growth as follows. After the Fe NWs were grown at $800\text{ }^\circ\text{C}$ for 30 min, the temperature was increased to $850\text{ }^\circ\text{C}$ at a ramping rate of $5\text{ }^\circ\text{C}/\text{min}$, while the other conditions were maintained. Subsequently, the growth of the NWs was continued for another 50 min, then the supply of FeCl_2 vapor was shut off, and the furnace was cooled to room temperature. The temperature program during the CVD is schematically shown in Figure 4(a). Figure S4 shows an SEM image of the NW grown by the two-step growth method. The diameter varied at the center of the NW. To observe the individual variation in the diameter and crystallographic

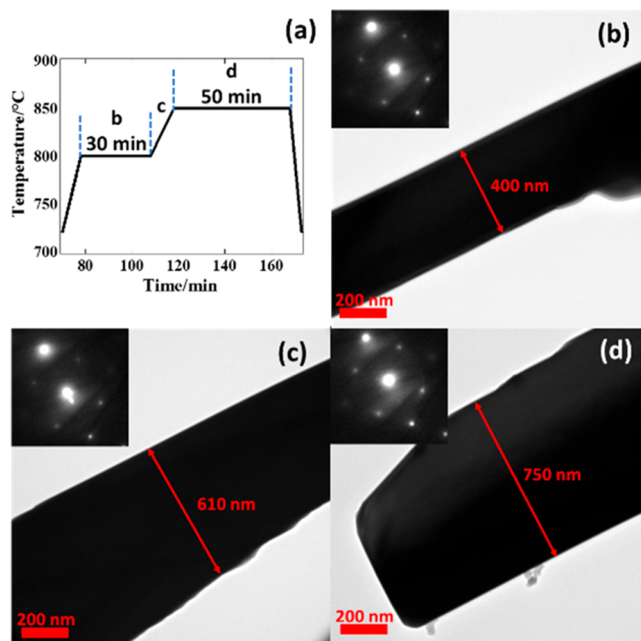


Figure 4. (a) Temperature program for the two-step growth method. (b–d) TEM images show the base (b), center (c), and tip (d) of the NW grown by the two-step growth method. The electron diffraction patterns in the insets illustrate no variation in the crystallographic orientation of a single NW.

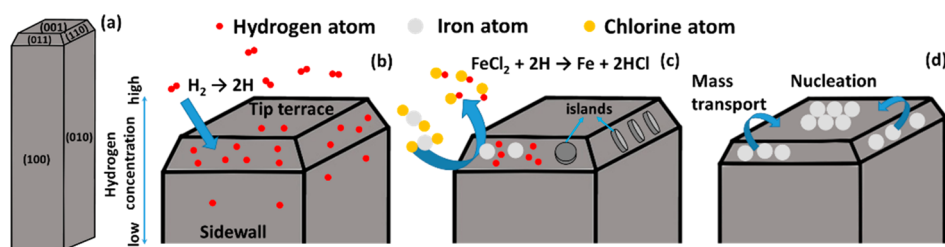


Figure 5. (a) Orientation of the Fe NW determined by TEM observation shown in Figure 3. (b) Preferable adsorption of dissociative hydrogen atoms on {110} surface due to the highest Fe–H binding energy among the low indexed planes. (c) Reduction of FeCl_2 on the surface of {110} and 2D island growth. (d) Mass transport from the tip rim to tip terrace and nucleation for the Fe NW growth.

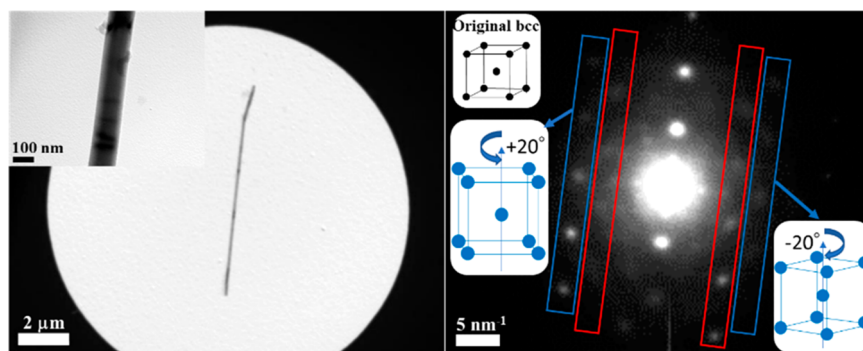


Figure 6. TEM image (left) and electron diffraction pattern (right) of an NW with a diameter of 100 nm. The center of the NW was magnified as shown in the inset (left) to see the diameter of the NW. The electron diffraction pattern includes two distinctive spots enclosed by the blue and red rectangles, which correspond to the bcc structure rotated $\pm 20^\circ$ and $\pm 25^\circ$ from the original bcc with a growth direction as an axis, respectively. A crystallographic relationship for the $\pm 20^\circ$ rotated structure is illustrated in the insets.

orientation at the base, center, and tip of the NW, TEM images and electron diffraction patterns were obtained as shown in Figure 4(b–d). The characteristic diameter varied from the base (400 nm) to tip (700 nm). The temperature dependence of the characteristic diameter was rationalized by the Ehrlich-Schwoebel barrier that prevents the step down of an adatom from terrace to terrace.^{29,31} Electron diffraction patterns clarified that the Fe NWs grew along the $\langle 100 \rangle$ direction, and there is no variation in the crystallographic orientation at the base, center, and tip as shown in the insets. When considering that the characteristic diameter is a monotonically increasing function, Figure 4(b–d) indicate that the growth mode of the Fe NW was tip growth, not base growth. It should be noted that it was difficult to make a plot of the temperature vs diameter in our experiment because the temperature range of the NWs growth was narrow. Almost nothing formed when the reaction temperature was 700 °C, and only chunks of Fe were generated when it was 1000 °C as shown in Figure S5.

Although the growth mechanism was experimentally determined, it is crystallographically curious that the Fe NWs were surrounded by {100} planes because the equilibrium shape (Wulff shape) of the bcc structure is surrounded by the {110} plane that is the most stable. Thus, another anisotropic effect for the Fe NW growth that is based on kinetics should be taken into account. We consider the reduction reaction that can be written as $\text{H}_2 + \text{FeCl}_2 \rightarrow \text{Fe} + 2\text{HCl}$ to discuss the mechanism. It can be assumed that the reaction includes three steps; i.e., (i) dissociative adsorption of a hydrogen molecule on the Fe surface, (ii) two adsorbed hydrogen atoms react with the FeCl_2 molecule adsorbed on the Fe surface, forming a (reduced) Fe atom and two HCl molecules, and (iii) the HCl molecules desorb from the Fe surface. Since it is well recognized that a hydrogen molecule dissociatively adsorbs

on the Fe surface both theoretically^{32,33} and experimentally,³⁴ step (i) is reasonable. Step (ii) is supported by the fact that the reactivity of a dissociatively adsorbed hydrogen is much greater than that of a hydrogen molecule.³⁵ This fact is consistent with the result that no Fe NW grew on the SiO_2/Si substrate without FeO nanoparticles. The desorption of HCl in step (iii) is consistent with no detection of Cl atoms by an EDS analysis.

Figure 5(a) illustrates the surrounding planes of a Fe NW, which were determined by observing Figure 3(b,c). To explain the growth of the Fe NWs, we suggest a plausible mechanism as shown in Figure 5(b–d). The hydrogen concentration becomes the highest at the tip rim due to the Berg effect.^{30,36} Besides, the {110} surface is more active than the {100} surface to dissociatively adsorb hydrogen (Figure 5(b)) because the Fe–H binding energy of {110} is the highest among the low indexed planes.³² Therefore, the reduction of FeCl_2 and 2D island growth of Fe preferentially takes place on the {110} surfaces (the truncated tip rim) as shown in Figure 5(c). The 2D island growth at the tip rim results in decreasing the surface area of the {110} planes and increasing that of the {100} planes. This 2D island growth causes the increase in the total surface free energy of the Fe NW because the surface free energy of the {110} plane is lower than that of the {100} plane. When the surface area of the {110} plane reaches a certain value, Fe atoms were transported to the main facet (001) to decrease the surface free energy, and nucleation occurs at the tip terrace (Figure 5(d)). Since the tip terrace was surrounded by four {110} planes, the collision rate of Fe atoms at the tip terrace was approximately four times larger than that at the sidewalls. Therefore, the nucleation took place more often at the tip terrace than sidewalls, which results in the uniaxial growth of a Fe NW. A similar NW growth process has been observed in the $\text{W}_{18}\text{O}_{49}$ NW grown by physical vapor

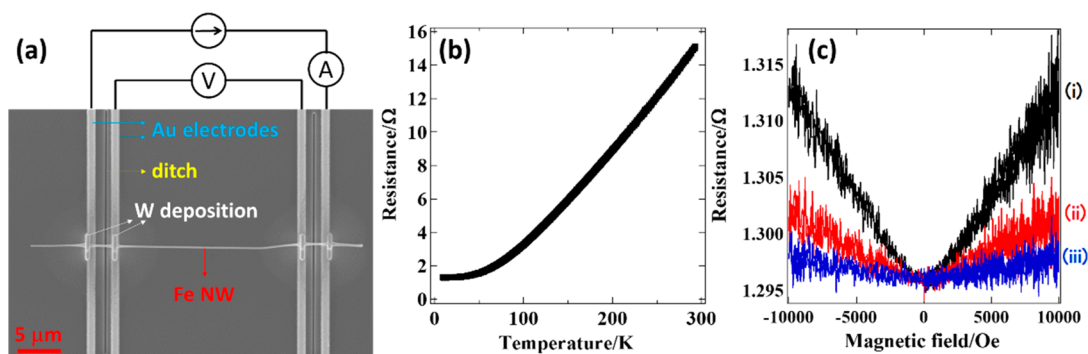


Figure 7. (a) SEM image of the sample geometry for 4-terminal sensing measurement. Four gold electrodes were prepared by the typical electron beam lithography. A single Fe NW was transferred onto the electrodes using a micromanipulator. W metal was deposited at the junction between the gold electrodes and the Fe NW to make good electrical contacts for the measurement. Ditches between the gold electrodes are necessary in order not to form a short circuit due to the W deposition. (b) Temperature dependency of resistance for the Fe NW. (c) Magnetoresistance of the Fe NW when the magnetic field was applied (i) perpendicular, (ii) 30 degrees, and (iii) parallel to the NW.

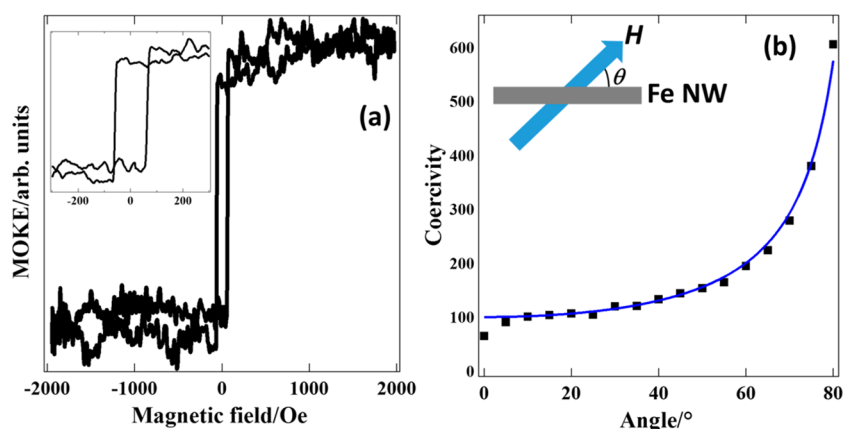


Figure 8. (a) MOKE signal when the magnetic field was applied perpendicular to the NW. Inset shows the expansion of the range from -300 to 300 Oe to observe the sharp flip of the magnetization. (b) Angle dependence of coercivity of the NW. The blue curve is fitted by $H_0/\cos \theta$.

deposition.³⁰ A high concentration of FeCl_2 at the tip due to the Berg effect is another reason why nucleation preferentially occurs at the tip terrace than the sidewall. Therefore, the $\{100\}$ planes at the sidewalls of the Fe NW do not contribute to the transverse growth, and only the tip is the growing point resulting in the NW shape.

We noticed that an NW with a diameter of approximately 100 nm was polycrystalline as shown in Figure 6. It is unusual for the polycrystalline NW to grow in one direction without a template. One possible reason to explain the polycrystalline NW growth is lowering the temperature of the martensitic transition (fcc-to-bcc phase transition). Although the temperature of the phase transition (fcc \rightarrow bcc) in bulk is 912 °C, a theoretical calculation predicts that the temperature of the phase transition becomes lower as the size is smaller.³⁷ In other words, NWs became polycrystalline (bcc phase) during cooling after the NWs grew as a single crystal in the fcc phase. The orientation of the NW is not completely random because the diffraction spots indicated by the blue and red rectangles in Figure 6 are assignable to ones when it is rotated $\pm 20^\circ$ and $\pm 25^\circ$ with the growth direction as an axis. The unusual orientation that is not a common habit plane in bulk^{38–41} is probably due to a sizable uniaxial anisotropy (NW shape) that causes different stress as compared to that of bulk. In order to make thinner single-crystal Fe NWs, a more suitable precursor such as an organometallic compound is needed to decrease the

growth temperature because Fe NWs could grow only at around 800 °C as long as FeCl_2 was used as the precursor.

The temperature dependence of the resistivity (R – T) for a single-crystal NW with a diameter of 450 nm was measured using a 4-terminal sensing method. The detailed geometry and preparation for the measurement are shown in Figure 7(a). Figure 7(b) shows the R – T curve in the range of 9 – 293 K. The residual resistance ratio (RRR) of the Fe NW (11.6) is greater than that (2 – 5) of the NWs synthesized by electrochemical deposition in the literature.^{42,43} This result clearly illustrates that the crystallinity of the Fe NWs grown by CVD is much better than that grown by electrochemical deposition. Considering only the diffusive scattering based on the Fuchs–Sondheimer model,⁴⁴ the residual resistance for the Fe NW with a diameter of 450 nm can be calculated as only 0.105 Ω (RRR = 136). The discrepancy between the experimental (1.30 Ω) and theoretical (0.105 Ω) values is probably due to the silicon impurity arising from the substrate because even ppm-order Si impurity that cannot be detected by EDS to reduce the RRR values.^{16,45} However, it should be noted again that the RRR of our Fe NW is much better than that grown by electrochemical deposition. Magnetoresistance (MR) measurements were carried out using the same geometry of the R – T measurement at 9 K with the NW oriented (i) perpendicular, (ii) 30 degrees, and (iii) parallel to the direction of the applied magnetic field as shown in Figure

7(c). The magnetic field was swept from 10 to -10 kOe and a constant dc current ($100 \mu\text{A}$) was in the growth direction $\langle 100 \rangle$. Two major contributions to the MR, ordinary (Lorentz) MR (OMR) and anisotropic (spin-orbit) MR (AMR), must be considered in a ferromagnet. When $\Delta R/R_0 = (R_{\parallel} - R_{\perp})/R_0$, where R_0 is the MR at a zero field, R_{\parallel} is the MR when the magnetic field is parallel to the current, and R_{\perp} is the MR when perpendicular, is defined as the MR ratio, the Lorentz force and spin-orbit effect yield $\Delta R/R_0 > 0$ and $\Delta R/R_0 < 0$, respectively.^{46,47} This fact shows that the OMR is a major factor in our Fe NW. According to ref 45, which reported the case of a thin film, $\Delta R/R_0$ becomes negative when the thickness is below 30 nm because the surface scattering limits the electron mean free path. Moreover, the AMR of the $\langle 100 \rangle$ direction is the lowest (less than 0.1%) among the three major axes ($\langle 100 \rangle$, $\langle 110 \rangle$, $\langle 111 \rangle$). Therefore, the AMR effect was not observed in our Fe NW due to the limitation of our measurement system (limit of resolution).

Figure 8(a) shows the magneto-optic Kerr effect (MOKE) signal of a single Fe NW at room temperature when the applied magnetic field was parallel to the growth direction of the Fe NW. The single Fe NW was transferred by a micromanipulator to a clean SiO_2/Si substrate to eliminate the contamination effect. The angle dependence of the magnetization for the 30, 60, 80, and 90 deg is shown in Figure S6, and the hysteresis loop finally disappeared when the applied magnetic field was perpendicular to the growth direction because the magnetization did not saturate in the maximum magnetic field (2000 Oe). The angle dependence of the coercivity was plotted every 5° in the range from 0° to 80° as shown in Figure 8(b). The blue curve was fitted by $H_0/\cos \theta$, where H_0 is the coercivity when the magnetic field is parallel to the growth direction of the NW and θ is the angle between the magnetic field and the NW (see the inset of Figure 8(b)). The well-fitting curve confirms that the magnetic response of the single-crystal Fe NW is almost ideal. H_0 was determined to be 110 Oe from the fitting curve, and this is much higher than that of bulk Fe (~ 1 Oe). The enhancement of the coercivity is due to the high aspect ratio of the Fe NW. The anisotropy field was calculated to be 11000 Oe for our Fe NW using the aspect ratio (30) and magnetization of the bulk α -Fe ($M_s = 1750 \text{ e.m.u. cm}^{-3}$), which is consistent with the result that the magnetization did not saturate at 2000 Oe when the magnetic field is perpendicular to the growth direction of the NW. The square ratio (M_r/M_s , where M_r and M_s are the residual magnetization and saturation magnetization, respectively) is roughly estimated from Figure 8(a) as 0.9, which is higher than that of the NWs grown by electrochemical deposition. Sharp flipping of the magnetization and $1/\cos \theta$ relation show no major domain-wall pinning site such as grain boundary and precipitate in the Fe NW, which means our Fe NW showed magnetic uniformity.

CONCLUSION

We have synthesized Fe NWs on SiO_2/Si substrates using FeO nanoparticles by the two-flow CVD. Electron diffraction, $R-T$ measurement, and MOKE measurement showed the excellent crystalline quality of the Fe NW grown by the CVD. The detailed observations of the morphology revealed that the Fe NW grew via the VS mechanism in the tip growth mode. The strong anisotropy of the magnetization for the Fe NW indicated that our CVD approach is suitable to make

nanostructured magnetic materials, such as the core-shell structure, with high quality and heterojunction.

ASSOCIATED CONTENT

Supporting Information

The Supporting Information is available free of charge on the ACS Publications website at DOI: 10.1021/acs.cgd.9b01148.

EDS and SEM images, surface morphologies, and angle dependence (PDF)

AUTHOR INFORMATION

Corresponding Author

*E-mail: yanase42@eng.hokudai.ac.jp.

ORCID

Takashi Yanase: 0000-0002-5625-9308

Takeshi Yanagida: 0000-0003-4837-5701

Kazuki Nagashima: 0000-0003-0180-816X

Notes

The authors declare no competing financial interest.

ACKNOWLEDGMENTS

Instrumental analyses were supported by the Nanotechnology platform at Hokkaido University by METI, Japan. T.Y. received financial support from the Nippon Sheet Glass Foundation for Materials Science and Engineering and JSPS KAKENHI Grant Number JP19K15386.

REFERENCES

- (1) Wagner, R.; Ellis, W. Vapor-liquid-solid Mechanism of Single Crystal Growth. *Appl. Phys. Lett.* **1964**, *4*, 89–90.
- (2) Tian, B.; Xie, P.; Kempa, T. J.; Bell, D. C.; Lieber, C. M. Single-Crystalline Kinked Semiconductor Nanowire Superstructures. *Nat. Nanotechnol.* **2009**, *4*, 824–829.
- (3) Alper, J.; Gutes, A.; Carraro, C.; Maboudian, M. Semiconductor Nanowires Directly Grown on Graphene—towards Wafer Scale Transferable Nanowire Arrays with Improved Electrical Contact. *Nanoscale* **2013**, *5*, 4114–4118.
- (4) Goldberger, J.; He, R.; Zhang, Y.; Lee, S.; Yan, H.; Choi, H.; Yang, P. Single-Crystal Gallium Nitride Nanotubes. *Nature* **2003**, *422*, 599–602.
- (5) Gudixsen, M.; Lauhon, L.; Wang, J.; Smith, D.; Lieber, C. Growth of Nanowire Superlattice Structures for Nanoscale Photonics and Electronics. *Nature* **2002**, *415*, 617–620.
- (6) Kuo, D.; Chang, B. From Preannealing of Bilayer Catalysts to Explore the Growth Micromechanisms of ZnO Nanorods. *Cryst. Growth Des.* **2010**, *10*, 977–982.
- (7) Hong, S.; Yeo, J.; Manorotkul, W.; Kang, H.; Lee, J.; Han, S.; Rho, Y.; Suh, Y.; Sung, H.; Ko, S. Digital Selective Growth of a ZnO Nanowire Array by Large Scale Laser Decomposition of Zinc Acetate. *Nanoscale* **2013**, *5*, 3698–3703.
- (8) Dayeh, S.; Yu, E.; Wang, D. III–V Nanowire Growth Mechanism: V/III Ratio and Temperature Effects. *Nano Lett.* **2007**, *7*, 2486–2490.
- (9) Clément, N.; Han, X.; Larrieu, G. Electronic Transport Mechanisms in Scaled Gate-All-around Silicon Nanowire Transistor Arrays. *Appl. Phys. Lett.* **2013**, *103*, 263504.
- (10) Qin, Y.; Liu, D.; Zhang, T.; Cui, Z. Ultrasensitive Silicon Nanowire Sensor Developed by a Special Ag Modification Process for Rapid NH_3 Detection. *ACS Appl. Mater. Interfaces* **2017**, *9*, 28766–28773.
- (11) Renitta, A.; Vijayalakshmi, K. High Performance Hydrogen Sensor Based on Mn Implanted ZnO Nanowires Array Fabricated on ITO Substrate. *Mater. Sci. Eng., C* **2017**, *77*, 245–256.

- (12) Park, S.; An, S.; Ko, H.; Jin, C.; Lee, C. Synthesis of Nanograined ZnO Nanowires and Their Enhanced Gas Sensing Properties. *ACS Appl. Mater. Interfaces* **2012**, *4*, 3650–3656.
- (13) Ebels, U.; Radulescu, A.; Henry, Y.; Piraux, L.; Ounadjela, K. Spin Accumulation and Domain Wall Magnetoresistance in 35 nm Co Wires. *Phys. Rev. Lett.* **2000**, *84*, 983–986.
- (14) Wegrowe, J.; Kelly, D.; Franck, A.; Gilbert, S.; Ansermet, J. Magnetoresistance of Ferromagnetic Nanowires. *Phys. Rev. Lett.* **1999**, *82*, 3681–3684.
- (15) Hassel, C.; Römer, F.; Meckenstock, R.; Dumpich, C.; Lindner, J. Magnetization Reversal in Epitaxial Fe Nanowires on GaAs (110). *Phys. Rev. B: Condens. Matter Mater. Phys.* **2008**, *77*, 224439.
- (16) Chan, K.; Kan, J.; Doran, C.; Ouyang, L.; Smith, D.; Fullerton, E. Oriented Growth of Single-Crystal Ni Nanowires onto Amorphous SiO₂. *Nano Lett.* **2010**, *10*, 5070–5075.
- (17) Arora, S.; O'Dowd, B.; McElligot, P.; Shvets, I.; Thakur, P.; Brookes, N. Magnetic Properties of Planar Arrays of Fe-Nanowires Grown on Oxidized Vicinal Silicon (111) Templates. *J. Appl. Phys.* **2011**, *109*, 07B106.
- (18) Pan, H.; Liu, B.; Yi, J.; Poh, C.; Lim, S.; Ding, J.; Feng, Y.; Huan, C.; Lin, J. Growth of Single-Crystalline Ni and Co Nanowires via Electrochemical Deposition and Their Magnetic Properties. *J. Phys. Chem. B* **2005**, *109*, 3094–3098.
- (19) Mohaddes-Ardabili, L.; Zheng, H.; Ogale, S.; Hannoyer, B.; Tian, W.; Wang, J.; Lofland, S.; Shinde, S.; Zhao, T.; Jia, Y.; Salamanca-Riba, L.; Schlom, D.; Wuttig, M.; Ramesh, R. Self-Assembled Single-Crystal Ferromagnetic Iron Nanowires Formed by Decomposition. *Nat. Mater.* **2004**, *3*, 533–538.
- (20) Chan, K. T.; Doran, C.; Shipton, E. G.; Fullerton, E. E. Core-Shell Structured Nanowire Spin Valves. *IEEE Trans. Magn.* **2010**, *46*, 2209–2211.
- (21) Gardner, R. Controlled Growth of α -Fe Single Crystal Whiskers. *J. Cryst. Growth* **1978**, *43*, 425–432.
- (22) Kittaka, S.; Kaneko, T. Growth of a Large Number of Iron Whiskers by the Reduction of Halides. *Jpn. J. Appl. Phys.* **1969**, *8*, 860–869.
- (23) Isin, A.; Coleman, R. Temperature Dependence of Magnetoresistance in Iron. *Phys. Rev.* **1966**, *142*, 372–378.
- (24) Yanase, T.; Kawahito, A.; Hashimoto, Y.; Endo, T.; Wang, Y.; Nagahama, T.; Shimada, T. Fe Whisker Growth Revisited: Effect of Au Catalysis for [02–1] Oriented Nanowires with 100 nm Diameter. *RSC Adv.* **2014**, *4*, 27620–27624.
- (25) Kawahito, A.; Yanase, T.; Endo, T.; Nagahama, T.; Shimada, T. Fabrication of Fe Nanowires on Yttrium-Stabilized Zirconia Single Crystal Substrates by Thermal CVD Methods. *J. Appl. Phys.* **2015**, *117*, 17D506.
- (26) Kern, W. The Evolution of Silicon Wafer Cleaning Technology. *J. Electrochem. Soc.* **1990**, *137*, 1887–1892.
- (27) Hou, Y.; Xu, Z.; Sun, S. Controlled Synthesis and Chemical Conversions of FeO Nanoparticles. *Angew. Chem.* **2007**, *119*, 6445–6448.
- (28) Hsu, Y.; Lu, S. Vapor-Solid Growth of Sn Nanowires: Growth Mechanism and Superconductivity. *J. Phys. Chem. B* **2005**, *109*, 4398–4403.
- (29) Shu, D.; Xiong, X.; Wang, Z.; Zhang, Z.; Wang, M.; Ming, N. Atomistic Mechanisms and Diameter Selection during Nanorod Growth. *J. Phys. Chem. C* **2011**, *115*, 31–36.
- (30) Zhang, Z.; Wang, Y.; Li, H.; Yuan, W.; Zhang, X.; Sun, C.; Zhang, Z. Atomic-Scale Observation of Vapor–Solid Nanowire Growth via Oscillatory Mass Transport. *ACS Nano* **2016**, *10*, 763–769.
- (31) Zhou, L.; Huang, H. Characteristic Length Scale of Nanorod Diameter during Growth. *Phys. Rev. Lett.* **2008**, *101*, 266102.
- (32) Wang, T.; Wang, S.; Luo, Q.; Li, Y.; Wang, J.; Beller, M.; Jiao, H. Hydrogen Adsorption Structures and Energetics on Iron Surfaces at High Coverage. *J. Phys. Chem. C* **2014**, *118*, 4181–4188.
- (33) Jiang, D.; Carter, E. Adsorption and Diffusion Energetics of Hydrogen Atoms on Fe (1 1 0) from First Principles. *Surf. Sci.* **2003**, *547*, 85–98.
- (34) Bozso, F.; Ertl, G.; Grunze, M.; Weiss, M. Chemisorption of Hydrogen on Iron Surfaces. *Appl. Surf. Sci.* **1977**, *1*, 103–119.
- (35) Gross, A. Hydrogen Dissociation on Metal Surfaces—a Model System for Reactions on Surfaces. *Appl. Phys. A: Mater. Sci. Process.* **1998**, *67*, 627–635.
- (36) Berg, W. Crystal Growth from Solutions. *Proc. R. Soc. A* **1938**, *7*, 79–95.
- (37) Sandoval, L.; Urbassek, H.; Entel, P. The Bain versus Nishiyama-Wassermann Path in the Martensitic Transformation of Fe. *New J. Phys.* **2009**, *11*, 103027.
- (38) Cayron, C. One-Step Model of the Face-Centred-Cubic to Body Centred-Cubic Martensitic Transformation. *Acta Crystallogr., Sect. A: Found. Crystallogr.* **2013**, *A69*, 498–509.
- (39) Ou, X. Molecular Dynamics Simulations of Fcc-to-Bcc Transformation in Pure Iron: a Review. *Mater. Sci. Technol.* **2017**, *33*, 822–835.
- (40) Ping, D.; Guo, S.; Imura, M.; Liu, X.; Ohmura, T.; Ohmura, M.; Lu, X.; Abe, T.; Onodera, H. Lath Formation Mechanisms and Twinning as Lath Martensite Substructures in an Ultra Low Carbon Iron Alloy. *Sci. Rep.* **2018**, *8*, 14264.
- (41) Sandoval, L.; Urbassek, H. Finite-Size Effects in Fe-Nanowire Solid-Solid Phase Transitions: A Molecular Dynamics Approach. *Nano Lett.* **2009**, *9*, 2290–2294.
- (42) Kamalakar, M.; Raychaudhuri, A.; Wei, X.; Teng, J.; Prewett, P. Temperature Dependent Electrical Resistivity of a Single Strand of Ferromagnetic Single Crystalline Nanowire. *Appl. Phys. Lett.* **2009**, *95*, 013112.
- (43) Rheem, Y.; Yoo, B.; Beyermann, W.; Myung, N. W. Magneto-transport Studies of Single Ferromagnetic Nanowire. *Phys. Status Solidi A* **2007**, *204*, 4004–4008.
- (44) Sondheimer, E. The Mean Free Path of Electrons in Metals. *Adv. Phys.* **1952**, *1*, 1–42.
- (45) Fujii, T.; Morimoto, I. Residual Resistivity of High Purity Iron. *Jpn. J. Appl. Phys.* **1969**, *8*, 1154–1158.
- (46) van Gorkom, R. P.; Caro, J.; Klapwijk, T. M.; Radelaar, S. Temperature and Angular Dependence of the Anisotropic Magnetoresistance in Epitaxial Fe Films. *Phys. Rev. B: Condens. Matter Mater. Phys.* **2001**, *63*, 134432.
- (47) Granberg, P.; Isberg, P.; Baier, T.; Hjörvarsson, B.; Nordblad, P. Anisotropic Behaviour of the Magnetoresistance in Single Crystalline Iron Films. *J. Magn. Magn. Mater.* **1999**, *195*, 1–8.